Received: 1 August 2019 | Revised: 23 December 2019 | Accepted: 6 January 2020 | Published on: 29 January 2020

DOI: 10.1002/qj.3745

Quarterly Journal of the Royal Meteorological Society RMetS

RESEARCH ARTICLE

Observational evidence of the preferential occurrence of wind convergence over sea surface temperature fronts in the Mediterranean

Agostino N. Meroni[1] | Michele Giurato[1] | Francesco Ragone[1,2] | Claudia Pasquero[1,3]

[1]Department of Earth and Environmental Sciences, University of Milano-Bicocca, Milan, Italy

[2]Laboratoire de Physique, ENS de Lyon, Université Claude Bernard, Lyon, France

[3]Institute of Atmospheric Sciences and Climate, Consiglio Nazionale delle Ricerche (ISAC-CNR), Turin, Italy

Correspondence
A. N. Meroni, Department of Civil and Environmental Engineering, Politecnico di Milano, Milan 20131, Italy.
Email: agostino.meroni@gmail.com

Funding information
DARFLIS project of Fondazione Cariplo and by the TWIGA project, funded from the European Union's Horizon 2020 Research and Innovation Programme, 776691

Abstract
Air and sea interact on a wide range of scales, shaping climate and influencing weather. The direct effect of sea surface temperature (SST) structures on the extratropical atmosphere at the daily time-scale is generally masked by the large variability associated with atmospheric dynamics. With 25 years of daily SST and surface wind observational products, obtained with data from buoys, satellite and atmospheric analysis in the Mediterranean, we show that strong surface wind convergence preferentially occurs when the air encounters a cold SST front. The mechanism responsible for the influence of ocean fronts on surface winds is rooted in the thermal disequilibrium that emerges at the air–sea interface, where cold water enhances the stability of the boundary layer, decoupling surface winds from the stronger winds aloft. Surface convergence drives upward motion which, under appropriate conditions, favours cloud formation. Thus, these results suggest that weather forecast models need to properly represent the small-scale ocean thermal structures, which could affect rainfall.

KEYWORDS
air–sea interactions, climatology, wind response

1 | INTRODUCTION

Recent development of high-resolution remote sensing of sea surface temperature (SST) and surface winds has stimulated research on the two-way interactions between atmosphere and oceans (Chelton and Xie, 2010). On large scales (>1000 km), a negative correlation has been observed between SST and wind magnitude (e.g., Xie, 2004). This is indicative of a passive behaviour of the ocean, which is cooled by the vertical mixing induced by the winds. However, at the mesoscale (10–1,000 km), there is instead observational evidence of a positive correlation (Liu *et al.*, 2000; Chelton *et al.*, 2001; Hashizume *et al.*, 2001). This indicates the control that the ocean has on the atmospheric boundary layer. In the presence of sharp SST gradients and mesoscale structures, the atmosphere does not have the time to fully adjust to the ocean temperature, which varies on much longer time-scales, and large air–sea thermal disequilibrium emerges. This implies that the SST modulates the surface air–sea heat fluxes (Businger and Shaw, 1984). Cold water enhances air column stability which decouples surface winds from the stronger winds aloft, and the opposite occurs for warm water. The oceanic signature can penetrate into the free troposphere and affect upward motion and precipitation, as indicated by the connections found between mesoscale SST structures and rainfall (Minobe *et al.*, 2008; Li and Carbone, 2012; Frenger *et al.*, 2013; Byrne *et al.*, 2015), lightning (Minobe *et al.*, 2010), and dramatic boundary-layer deepening (Messager and Swart, 2016).

The ocean mesoscale can affect the atmospheric boundary layer through the influence of the surface oceanic currents on the surface stress and winds, a process known as the Current Feedback (CFB), and through the effects that the SST field has on the surface wind, known as the Thermal Feedback (TFB), as summarised, for example, by Renault *et al.* (2019). In the present study the focus is on the surface wind divergence response to the SST spatial structure. It has been shown that the CFB mainly affects the wind curl response (Renault *et al.*, 2019) and thus only the TFB is studied here.

Through appropriate mesoscale-resolving ocean–atmosphere coupled numerical simulations, Renault *et al.* (2019) calculate all the coupling coefficients that are commonly introduced in the literature to measure the strength of the air–sea coupling. These coupling coefficients are the linear regression coefficients between some pairs of variables, such as surface wind (stress) and SST, wind (stress) divergence and downwind SST gradient, and wind (stress) curl and crosswind SST gradient. In this work, we analyse the relationship between SST and wind-derived variables through the calculation of various correlation coefficients.

Correlations between SST and winds have been found in many studies using observational data in regions with long-lived oceanic structures characterised by steep SST gradients, such as mesoscale eddies (Bourras *et al.*, 2004; Frenger *et al.*, 2013; Sun *et al.*, 2016) and western boundary current fronts and rings (Park *et al.*, 2006; Song *et al.*, 2006; Messager *et al.*, 2012; O'Neill *et al.*, 2012; Ma *et al.*, 2015; Rouault *et al.*, 2016). Usually, the correlations emerge considering the wind averaged over weekly or seasonal time-scales (Xie *et al.*, 1998; O'Neill *et al.*, 2005; Minobe *et al.*, 2008; Bryan *et al.*, 2010; Chelton and Xie, 2010; Roberts *et al.*, 2016; Wang and Castelao, 2016). Notable exceptions are the recent works of O'Neill *et al.* (2017), Seo (2017), and Gaube *et al.* (2019). The latter find evidence of the SST–wind relationship at kilometric and sub-kilometric spatial scales, with cutting-edge satellite measurements of wind speed and SST from a case-study along the Gulf Stream frontal system. O'Neill *et al.* (2017) find that the surface atmospheric boundary layer responds to the presence of a SST gradient on daily scales, and the response critically depends on the relative direction of the wind and the SST gradient. Seo (2017) shows the daily highpass filtered SST–wind link on the global scale and highlights that the correlations are higher over regions with strong mesoscale activity. The atmospheric response to SST structures has also been shown to influence cloud cover and rain rate (Frenger *et al.*, 2013).

The topic has stimulated several modelling and theoretical studies at the submesoscale, both in idealised and in realistic set-ups (De Szoeke and Bretherton, 2004; Skyllingstad *et al.*, 2007; Spall, 2007; Small *et al.*, 2008; Kilpatrick *et al.*, 2014; Byrne *et al.*, 2015; Meroni *et al.*, 2018; Renault *et al.*, 2018; Wenegrat and Arthur, 2018). Particular attention has been devoted to the role that SST structures have on heavy precipitation events in the Mediterranean, where widespread coastal urbanisation leads to large exposure of population and infrastructure to intense weather events. While the total amount of rain is not influenced much by the spatial resolution of the SST forcing field (Millán *et al.*, 1995; Pastor *et al.*, 2001; Lebeaupin *et al.*, 2006; Cassola *et al.*, 2016), numerical studies show that the spatial structure of the heat fluxes and the position of the rain bands can be influenced (Katsafados *et al.*, 2011; Ricchi *et al.*, 2016; Rainaud *et al.*, 2017; Meroni *et al.*, 2018; Iizuka and Nakamura, 2019). The landward moisture fluxes can also be influenced by the mesoscale SST structures on seasonal scales, as shown by the numerical work of Desbiolles *et al.* (2018). All these works suggest that a proper representation of air–sea interaction is required in order to obtain reliable forecasts of precipitation.

In the attempt to explain the physics of the TFB, i.e. how the ocean SST fronts influence the atmospheric boundary layer, two mechanisms have previously been identified. In the pressure adjustment (PA) mechanism (Lindzen and Nigam, 1987), the presence of a maximum in the SST induces an atmospheric pressure low, which generates surface convergence and a secondary circulation across SST gradients. In the downward momentum mixing (DMM) mechanism (Hayes *et al.*, 1989; Wallace *et al.*, 1989), when an air parcel crosses a SST front going from warm to cold water, its buoyancy decreases, static stability increases, and surface winds, strongly limited by friction, decouple from the free troposphere. The resulting net effect is a deceleration of the surface wind on the cold side of the front and, consequently, the generation of a convergence line along the front itself. Figure 1 shows schematically how the DMM mechanism works. The relative importance of the two mechanisms (PA and DMM) depends on cross-frontal wind velocity with respect to the front size (Spall, 2007; Small *et al.*, 2008; Foussard *et al.*, 2019) and on the boundary-layer stability (Foussard *et al.*, 2019). The two mechanisms have a different signature in the surface wind field, $\mathbf{u}$: while PA generates winds across SST gradients (∇SST), dominance of the DMM would imply positive correlations between surface winds and SST anomalies. Also, PA produces convergence on warm SST patches (on maxima of SST), and DMM produces convergence on crosswind fronts, when the scalar product between wind vector and SST gradient is negative ($\mathbf{u} \cdot \nabla$SST< 0), that is, an air parcel travelling

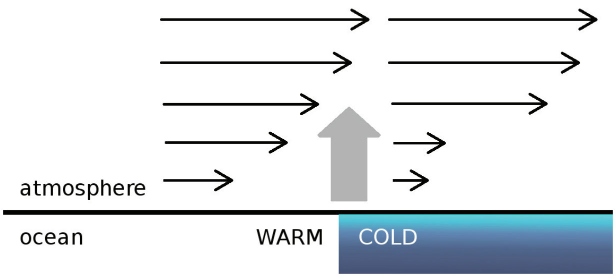

FIGURE 1 Schematic showing how the increased air stability near a SST front while going from warm to cold reduces the vertical mixing of horizontal momentum. The net effect is a deceleration of the surface wind that generates convergence and, very likely, upward motion (light grey arrow). In this figure $\mathbf{u} \cdot \nabla$SST< 0, and $\nabla \cdot \mathbf{u} < 0$ [Colour figure can be viewed at wileyonlinelibrary.com]

with the surface wind moves from a higher to a lower SST.

The purpose of this work is to investigate the physical mechanisms that link the SST field to the surface wind on daily time-scales. In particular, we want to demonstrate that the numerical results that underline the fast response of the wind to SST fronts over daily and sub-daily scales (e.g., Meroni *et al.*, 2018) are indeed supported by observational data, properly treated and analysed. The use of daily data is particularly relevant to study the effects that SST fronts have on the dynamics of a single weather event, which could not be investigated using monthly averages. We aim at verifying whether SST gradients can affect strong wind convergence, typically associated with atmospheric fronts embedded in low pressure synoptic systems, or whether the effects of ocean fronts are manifest only when the weather conditions are benign. In Section 2 we introduce the datasets used for the study. In Section 3 we describe the atmospheric response to SST structures in terms of surface wind convergence, presenting the analysis carried out in the work. Section 4 discusses the reasons why the atmospheric response to the SST is not visible at the daily scale by looking at the correlation between wind speed and SST. Section 5 then draws the conclusions of the work, highlighting the importance of a proper representation of the SST in weather forecasts.

2 | DATA

To investigate the effects of SST structures on the atmospheric boundary layer, we use 25 years of Mediterranean daily SST (OISST; Banzon *et al.*, 2016) and wind data (CCMPv2.0; Atlas *et al.*, 2011; Scott *et al.*, 2016), from 1990 to 2014, both available on a grid with spatial resolution of 0.25°.

The SSTs are obtained from the NOAA daily Optimum Interpolation Sea Surface Temperature dataset (OISST; https://www.ncdc.noaa.gov/oisst; accessed 13 January 2020). It is an analysis product that combines observations coming from satellites, ships and buoys, at a daily time step and 0.25° resolution on a regular grid (Banzon *et al.*, 2016). The Advanced Very High Resolution Radiometer (AVHRR) is the relevant satellite SST sensor in this dataset.

The V2.0 Cross-Calibrated Multi-Platform (CCMP) analysis product provides the ocean surface equivalent neutral winds, at the height of 10 m every 6 hr on the same regular 0.25° grid as the Optimum Interpolation Sea Surface Temperature (OISST; Atlas *et al.*, 2011; Wentz *et al.*, 2015). A Variational Analysis Method (VAM; Hoffman *et al.*, 2003) is used to merge various Remote Sensing System data (the radiometer wind speed of SSM/I, SSMIS, AMSR, TMI, WindSat and GMI and the scatterometer wind vectors of QuickSCAT and ASCAT) with moored buoy data, and ERA-40 reanalysis and the ECMWF operational analysis (Atlas *et al.*, 2011).[1]

The SST data have daily resolution while wind data have a 6 hr time step. In the analysis presented here, the winds at 0000 UTC have been used, but it was verified that very similar results are obtained for winds at different times of the day and for daily averaged winds.

SST and wind data have been used only over the common time period 1990–2014, and they have been taken over the Mediterranean Sea only. It should be noted that a lot of wind systems along the Mediterranean coasts are associated with the steep orography surrounding the basin (Zecchetto and Cappa, 2001). To avoid including the sea–land breeze and other coastal dynamic features of the wind field in the current analysis, a band two grid steps wide (roughly 50 km) is removed along the entire coastline of the Mediterranean Sea. The results are insensitive to the exact width of this band in the range from 1 to 5 grid steps (roughly 25 to 125 km, not shown). We highlight that the fact that the SST and wind datasets come from different instruments and processing methods means that the energy and mass balances at the air–sea interface might not be strictly closed. The independence of the two observational products implies that the correlations found in the present work are truly physical and are not a byproduct of a common data treatment. Since the resolution of the datasets is 0.25°, the daily and sub-daily control of the SST on the surface wind is studied with an effective resolution of $\mathcal{O}(100)$ km. The numerical work of Meroni *et al.* (2018)

[1]ECMWF=European Centre for Medium-range Weather Forecasts. ERA-40= 40-year reanalysis from ECMWF. SSM/I=Special Sensor Microwave Imager. SSMIS=Special Sensor Microwave Imager/Sounder. AMSR=Advanced Microwave Scanning Radiometer. TMI= the Tropical Rainfall Measuring Mission Microwave Imager. GMI=Global Precipitation Measurement Microwave Imager. QuikSCAT=Quick Scatterometer. ASCAT=Advanced Scatterometer.

shows that the SST–wind relationship dominated by the DMM mechanism gets stronger for increasing resolution in the range 1–100 km. Thus, anticipating the main outcomes of the present analysis, the results of this work are expected to become more relevant at smaller scales.

3 | THE LINKS BETWEEN SURFACE WIND CONVERGENCE AND SST FRONTS

We calculate both spatial and temporal correlation coefficients (as defined in detail in the Appendix) between three pairs of variables from the datasets, indicated by $\rho_s[a, b]$ and $\rho_t[a, b]$, respectively, with a and b denoting the two variables of interest. To characterise the DMM mechanism, the correlation coefficients between wind divergence, $\delta = \nabla \cdot \mathbf{u}$, and the scalar product between wind and SST gradient, $\gamma = \mathbf{u} \cdot \nabla \text{SST}$, are calculated. Using the spherical coordinates $\{\varphi, \theta\}$ over a sphere of radius $R = 6371$ km, where φ is the longitude and θ is the latitude, surface wind divergence is

$$\delta = \nabla \cdot \mathbf{u} = \frac{1}{R\cos\theta}\frac{\partial u}{\partial \varphi} + \frac{1}{R\cos\theta}\frac{\partial}{\partial \theta}(v\cos\theta), \tag{1}$$

with u and v being the eastward and northward wind components, respectively, and the SST rate of change experienced by an air parcel moving with the surface wind is

$$\gamma = \mathbf{u} \cdot \nabla \text{SST} = \frac{u}{R\cos\theta}\frac{\partial \text{SST}}{\partial \varphi} + \frac{v}{R}\frac{\partial \text{SST}}{\partial \theta}. \tag{2}$$

The quantity γ is the effective SST rate of change felt by the single air parcel during its motion. Its sign is determined by the relative direction of the instantaneous wind and the SST gradient.

The correlation coefficients between wind speed $|\mathbf{u}|$ and SST, and wind divergence and SST Laplacian are also calculated. The Laplacian of the SST is explicitly

$$\Lambda = \nabla^2\text{SST} = \frac{1}{R^2\cos^2\theta}\frac{\partial^2\text{SST}}{\partial \varphi^2} + \frac{1}{R^2\cos\theta}\frac{\partial}{\partial \theta}\left(\frac{\partial \text{SST}}{\partial \theta}\cos\theta\right), \tag{3}$$

and a positive correlation between SST Laplacian and wind divergence is indicative of the action of the PA mechanism, as mentioned in the Introduction.

The advantage of calculating both temporal and spatial coefficients lies in the fact that different mean values are subtracted in the two cases. When computing ρ_s, anomalies are calculated with respect to the instantaneous spatial mean; thus spatially averaged long-term trends and seasonal cycles are eliminated. On the other hand, temporal correlations are calculated for each month separately by computing the anomalies at each location with respect to their point-wise climatological monthly mean. Thus, any spatial structure at the regional or even the basin scale is removed.

We highlight again that the use of daily data allows us to study the effects of the SST structure on single storms, which is impossible with longer time-averaged data. This becomes clear when looking at the differences between a snapshot and a climatology of the fields under study. Figures 2 and 3 show, respectively, an instantaneous map at 0000 UTC on 12 October 2014 (a random October day from the whole dataset) and the climatological values for the month of October for all the fields of interest. In particular, wind speed, SST, surface wind divergence, SST gradient, dot product between wind and SST gradient, and SST Laplacian are shown. Note that, to allow a direct comparison between the two figures, the colourbar for a given variable is the same. It is worth noticing that, as highlighted for example by O'Neill *et al.* (2017), the climatological surface wind divergence is an order of magnitude lower than its instantaneous values when a storm is present. Thus, the use of monthly averages prevents us from studying the effects that SST has on the response of single weather events, which are often characterised by intense values of surface convergence.

When considering directly SST and surface wind, a mean negative correlation emerges (Figures 4b and 5b). While the negative spatial correlation probably reflects the fact that the SST has a latitudinal gradient and that the most intense winds are typically found in the northern basin (e.g., in the Gulf of Lion; Figure 3a,b), the negative temporal correlation indicates that strong winds trigger upper-ocean processes (upwelling and mixing) that generate negative thermal anomalies even at those short time-scales, while typically the ocean has a slower reaction. This result is consistent with what is shown by Seo (2017), who finds the negative correlation at these spatio-temporal scales to be a peculiarity of the Mediterranean region, while most of the rest of the globe, especially the regions with large oceanic variability, has positive correlations. By investigating the seasonality of the correlation coefficients, we notice that the negative values are particularly evident during summer (Figure 4e), when the mixed-layer base is very shallow and the stratification underneath is very strong (D'Ortenzio *et al.*, 2005). In these conditions, even a relatively short-lived wind gust is able to significantly reduce the SST, resulting in a negative correlation. The correlation between wind speed and SST being close to zero for the rest of the year, instead might be mostly related to the synoptic-scale activity and a relatively deeper mixed layer (D'Ortenzio *et al.*, 2005). Further analysis on the role of the oceanic stratification is needed to support this hypothesis, but since it goes beyond the scope of the present work, it is left for the future.

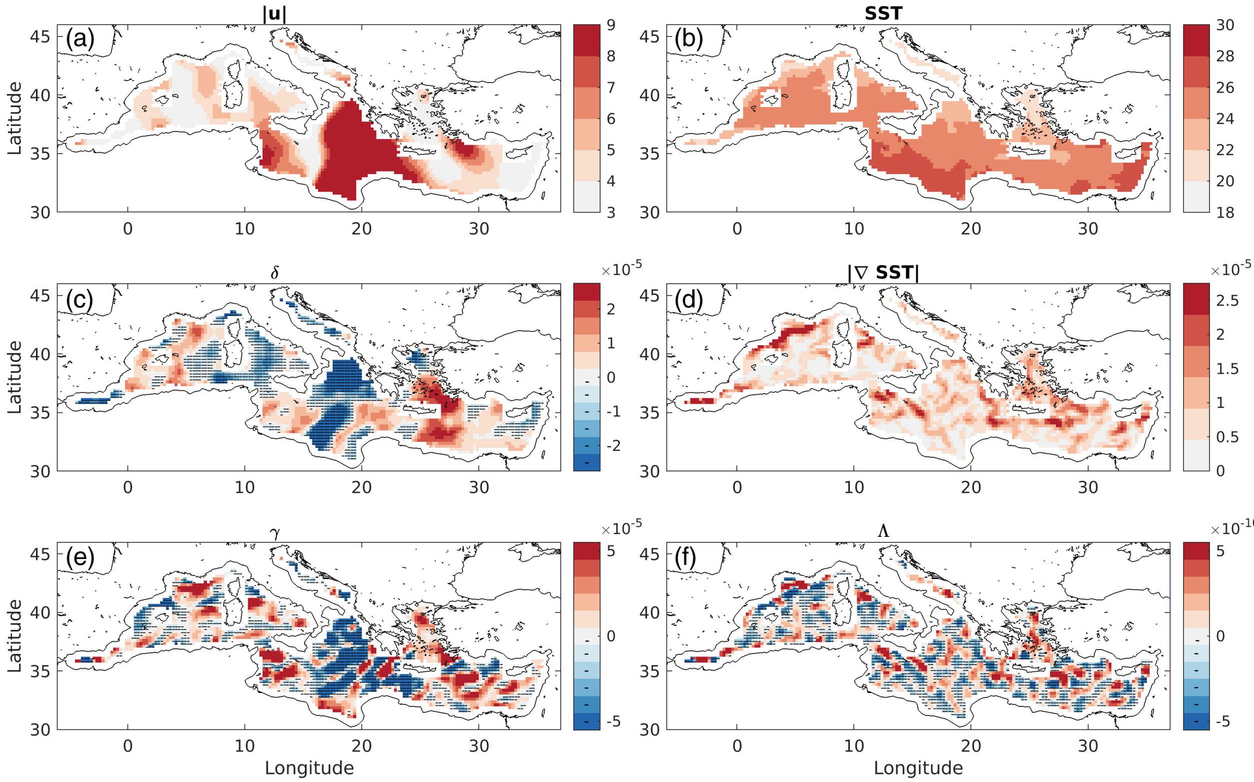

FIGURE 2 Instantaneous fields on 12 October 2014: (a) wind speed ($|\mathbf{u}|$, m·s^{-1}), (b) SST (°C), (c) surface wind divergence ($\delta = \nabla \cdot \mathbf{u}$, s^{-1}), (d) magnitude of the SST gradient ($|\nabla$SST$|$, K·m^{-1}), (e) dot product between wind and SST gradient (γ, K·s^{-1}), and (f) SST Laplacian (Λ, K·m^{-2}). Negative values are hatched with horizontal lines [Colour figure can be viewed at wileyonlinelibrary.com]

In summary, the analysis of the correlations between SST and surface wind speed in the Mediterranean does not provide evidence of an atmospheric response to SST anomalies.

The relevance of the DMM mechanism becomes evident when looking at the correlation between surface wind divergence and the downwind SST gradient. Figure 4d shows the climatological seasonal cycle of the spatial correlation coefficient between δ and γ, with a daily resolution. For most of the year, the correlations are generally positive, indicating a preference for convergence (divergence) when SST gradients are aligned with the wind and the wind goes from warm to cold (cold to warm) waters, in accordance with the DMM mechanism. From January to April, the mean correlation coefficient is roughly constant. It reaches its minimum in summer and its maximum in autumn. The seasonal differences are also visible in Figure 4a, where the histograms of the spatial correlation coefficients calculated for four different months of the year are shown. It should be noticed that during autumn strong SST gradients form due to the presence of a shallow seasonal thermocline removed by wind-induced mixing and buoyancy losses, which transform vertical gradients into horizontal ones (not shown).

Figure 4c,f shows that the spatial correlation coefficient between SST Laplacian and surface wind divergence is low and non-significant throughout the year. Also the temporal correlation coefficient between SST Laplacian and surface wind divergence is found to be low and non-significant, as shown in Figure 5c for the autumn season.

The climatological correlation coefficients of Figure 4 have also been calculated for the monthly averaged quantities, with the aim of relating the present work with previous results shown in the literature (e.g., Small *et al.*, 2008; Chelton and Xie, 2010; O'Neill *et al.*, 2017). These works highlight that, on average, the surface wind responds to mesoscale SST structures by accelerating over the warm side of the fronts (Small *et al.*, 2008; Chelton and Xie, 2010). With the appropriate considerations (for example the absence in the Mediterranean of a persistent and strong SST gradient that characterises the western boundary currents, and the relatively shallower ocean mixed layer, as discussed above), there is agreement with previous results. For this reason, and because various papers highlight the importance of the wind response at daily time-scales (O'Neill *et al.*, 2017; Plougonven *et al.*, 2018), they are not discussed here in detail.

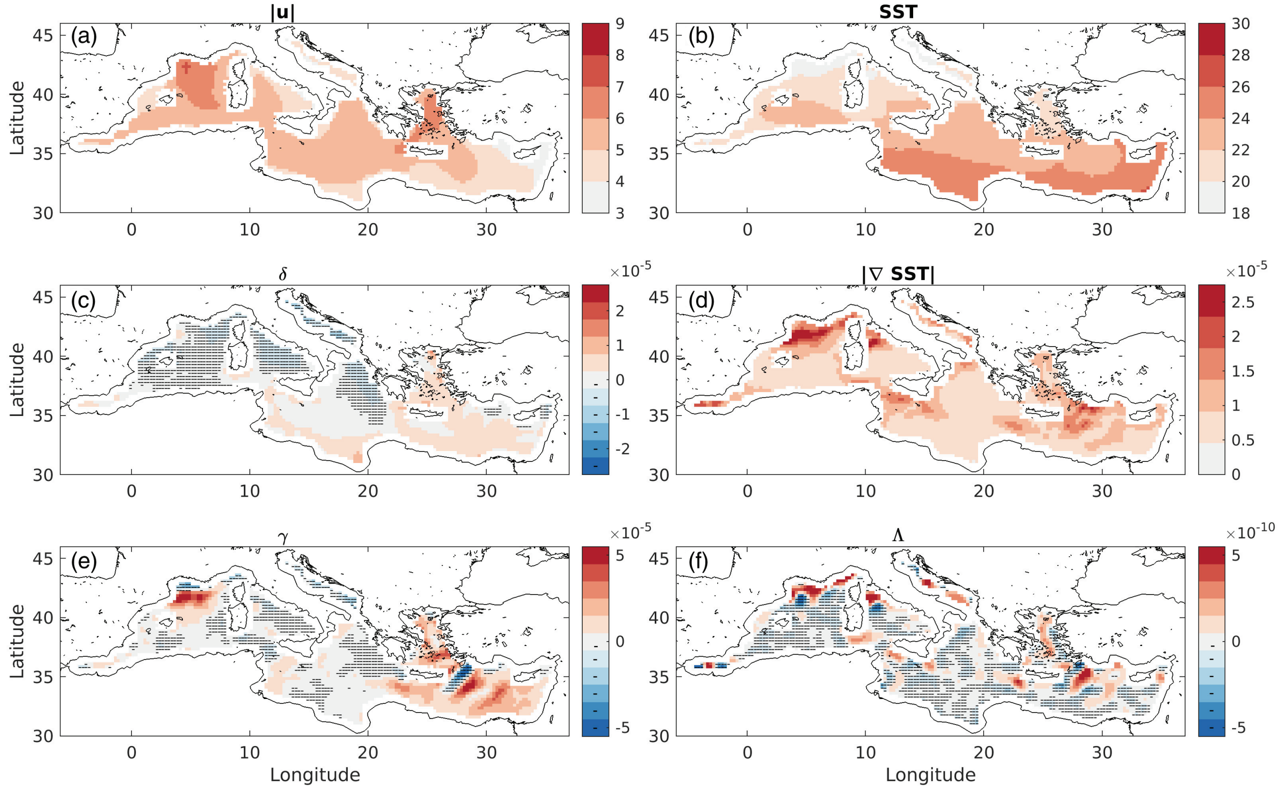

FIGURE 3 As Figure 2, but showing climatological fields for the month of October calculated between 1990 and 2014. [Colour figure can be viewed at wileyonlinelibrary.com]

Figure 5a shows the map of the temporal correlation coefficients between γ and δ calculated for the autumn season (SON). The correlation is positive and significant in most of the basin, suggesting that the DMM mechanism plays a considerable role in shaping convergence patterns. Although the values of the correlation coefficients shown here are large for some regions and seasons, on average the correlation is relatively low, $\mathcal{O}(0.1)$. Nevertheless, this value is statistically significant and it shows that, despite the large and certainly dominant source of variability related to the internal atmospheric dynamics, SST spatial structure impacts air–sea fluxes and modifies surface winds. The low and non-significant values of the correlation coefficients between surface wind divergence and the SST Laplacian (Figure 5c) suggests that the PA mechanism is not important over the spatio-temporal scales considered in the present work. However, no definitive conclusion can be drawn with the datasets used in this study, as we cannot assess the role of advection, which has been shown to break the correlation between surface wind divergence and the SST Laplacian (Song *et al.*, 2006; Foussard *et al.*, 2019).

To explicitly verify that the presence of SST fronts that are crossed from warm to cold induces surface convergence in the atmosphere, some conditional probability density functions (pdfs) are estimated from the entire datasets. In particular, the conditional pdfs of the downwind SST rate of change conditioned on the occurrence of surface wind divergence ($\delta > 0$) and surface wind convergence ($\delta < 0$), and the conditional pdfs of the surface wind divergence, conditioned on the presence of a front crossed from warm to cold ($\gamma < 0$) and a front crossed from cold to warm ($\gamma > 0$) are computed.

Figure 6 shows the normalised conditional pdfs of the downwind SST rate of change γ, $P(\gamma|\delta < 0)$ (conditioned on the presence of surface wind convergence, displayed as a solid line) and $P(\gamma|\delta > 0)$ (conditioned on surface wind divergence, dashed line), calculated for four months: January, April, July and October, in (a), (b), (e) and (f), respectively. In the case of wind divergence, both the mean downwind SST rate of change (indicated by the vertical dashed line) and the skewness of the distribution are positive at all times, while the same is not true in the case of wind convergence. To better visualise the differences in the two distributions, the ratio between them is introduced, namely

$$r(\gamma) = \frac{P(\gamma|\delta < 0)}{P(\gamma|\delta > 0)}. \quad (4)$$

Figure 6c,d,g,h show $r(\gamma)$ for the same months presented above. These ratios are typically larger (smaller) than the one for negative (positive) downwind SST rates of

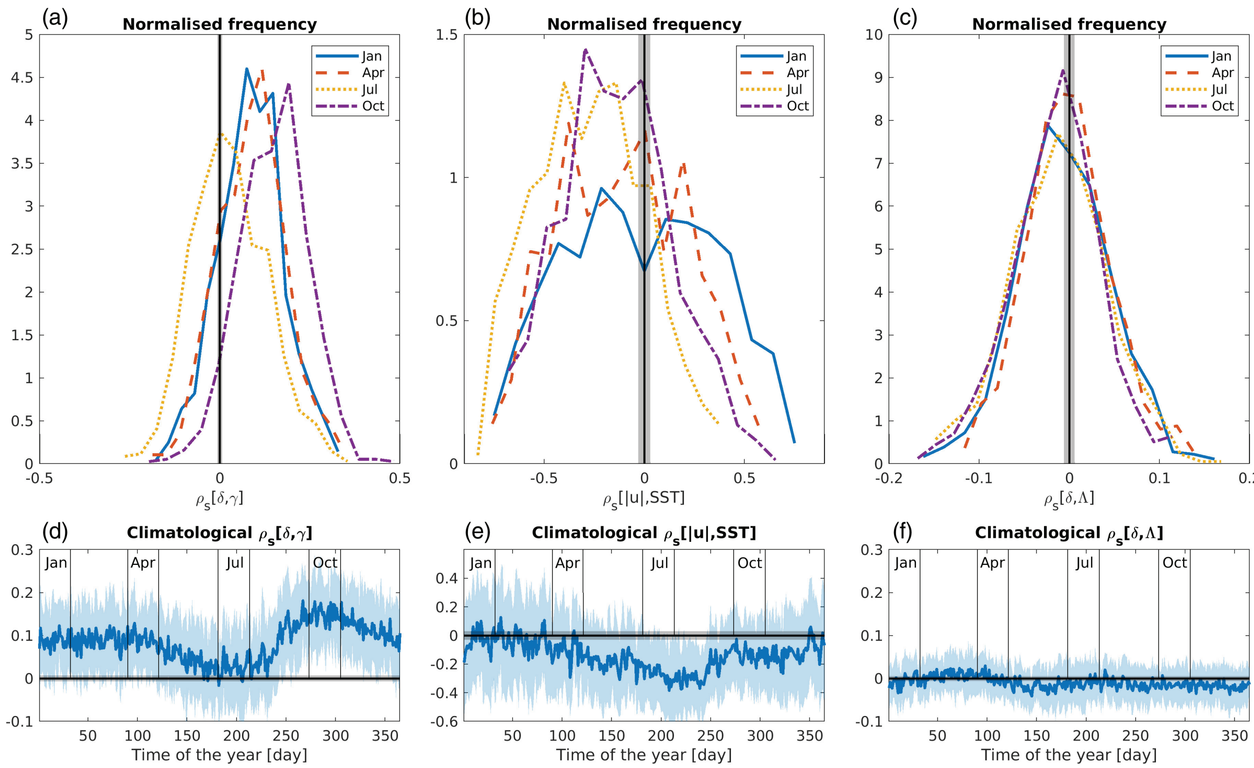

FIGURE 4 (a) Histograms of the spatial correlation coefficients, ρ_s, between surface divergence, defined in Equation (1) and denoted by δ, and the SST rate of change felt by an air parcel moving with the surface wind, defined in Equation (2) and denoted by γ, for four different months (January, April, July, October). (b, c) are as (a), but for (b) SST and wind speed, and (c) for surface divergence δ and SST Laplacian, defined in Equation (3) and denoted by Λ. (d, e, f) show the seasonal cycle of mean climatological spatial correlation coefficient calculated over 25 years for (d) δ and γ, (e) $|\boldsymbol{u}|$ and SST, and (f) δ and Λ. An interval of one standard deviation is highlighted by the shading area. In all the panels, the width of the line corresponding to $\rho_s = 0$ includes the 95% confidence interval for the null hypothesis of zero correlation [Colour figure can be viewed at wileyonlinelibrary.com]

change. Considering the month of October, for instance, and focusing on strong negative downwind SST rates of change, one can notice that the pdf conditioned on the cases of wind convergence is about twice as large as the one conditioned on the cases of wind divergence ($r(\gamma) \simeq 2$), while it becomes half of the latter ($r(\gamma) \simeq 0.5$) for strong positive SST gradients. This means that, over a strong SST gradient crossed from warm to cold, it is more likely to have surface wind convergence than divergence. In the Mediterranean region, wind divergence is encountered more often than convergence. Among the reasons for this, there is the fact that extratropical cyclones are more compact and affect a smaller area than anticyclones. The fact that wind divergence is more frequent than convergence is shown by the ratio of the non-normalised distributions, namely

$$r_{\mathrm{NN}}(\gamma) = \frac{F(\gamma|\delta < 0)}{F(\gamma|\delta > 0)}, \tag{5}$$

where $F(\gamma|\delta < 0)$ is the histogram of the observed downwind SST rate of change, conditioned on the presence of convergence, and $F(\gamma|\delta > 0)$ is the same for divergence. The relationship between $F(\gamma|\delta < 0)$ and $P(\gamma|\delta < 0)$ is simply

$$P(\gamma|\delta < 0) = \frac{F(\gamma|\delta < 0)}{\int_{-\infty}^{+\infty} F(\gamma|\delta < 0)\,\mathrm{d}\gamma}. \tag{6}$$

The ratio $r_{\mathrm{NN}}(\gamma)$ differs from the ratio $r(\gamma)$ only by a multiplicative constant, which is the ratio of the number of occurrence of surface convergence divided by the number of occurrence of surface divergence. The fact that $r_{\mathrm{NN}}(\gamma) < r(\gamma)$ means that there is a higher frequency of occurrence of surface divergence than surface convergence. Despite this bias, however, if we look at the autumn season which is characterised by intense storm activity, over strong fronts crossed from warm to cold, the chances of having surface wind convergence are about 50% higher ($r_{\mathrm{NN}}(\gamma) \simeq 1.5$) than having surface wind divergence. We interpret this result as the manifestation of the effect that ocean fronts have on near-surface winds.

In a similar way, Figure 7 shows the pdfs of wind divergence conditioned on the presence of a front crossed from warm to cold (solid line, $\gamma < 0$) or from cold to warm (dashed line, $\gamma > 0$), together with their corresponding ratios $r(\delta)$ and $r_{\mathrm{NN}}(\delta)$. In Figure 7a,b,e,f, one can notice that

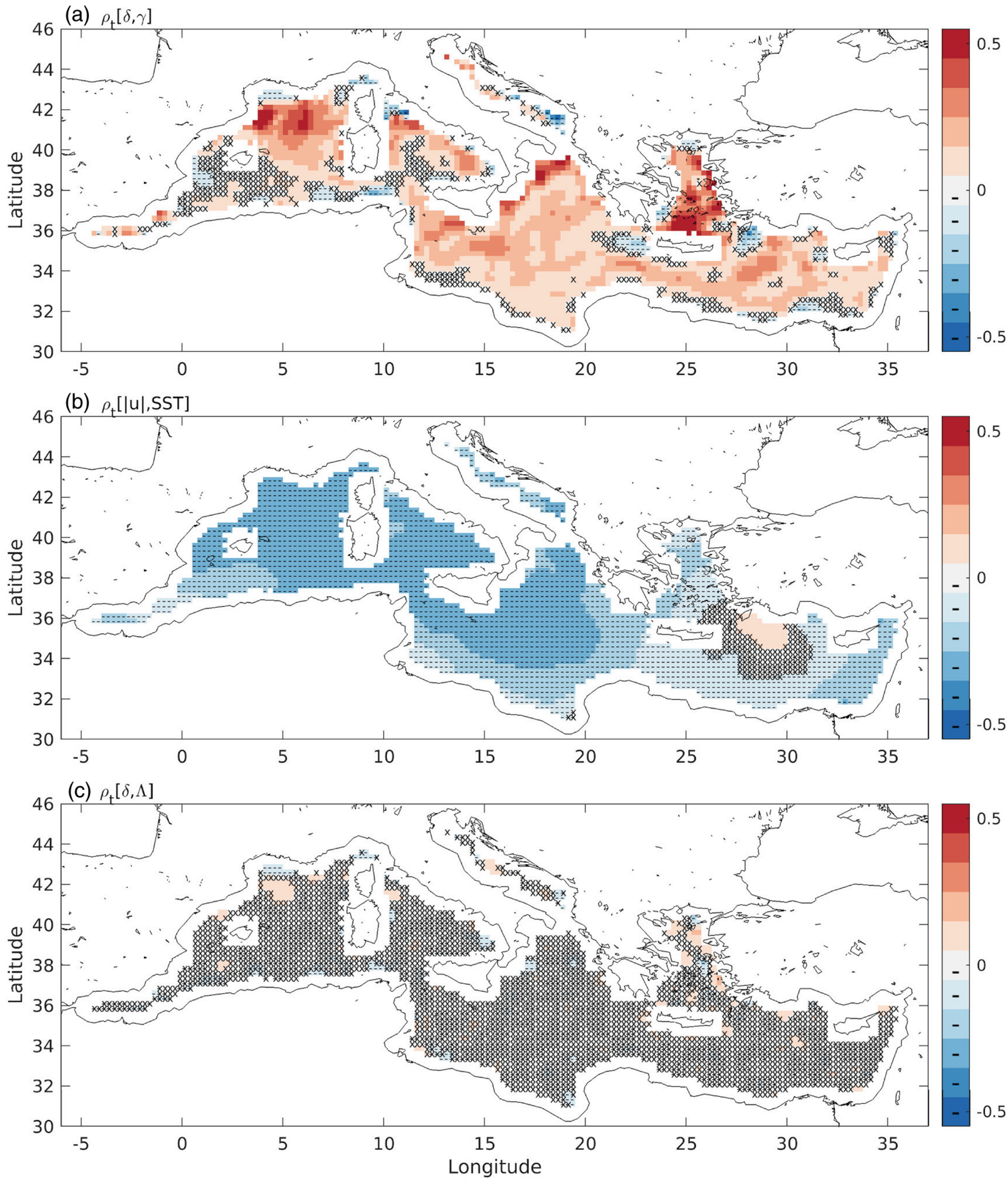

FIGURE 5 Temporal correlation coefficients ρ_t for the autumn season (SON) between (a) the surface wind divergence and the downwind SST gradient, (b) wind speed and SST, and (c) surface wind divergence and SST Laplacian. The non-significant values are denoted by an x symbol. The dash symbol denotes negative values [Colour figure can be viewed at wileyonlinelibrary.com]

the distributions have high tails on the negative side, indicating that convergence reaches larger values than divergence, and large values of convergence are more likely than large values of divergence. This is related to the fact that extratropical cyclones are more intense and compact than anticyclones and, in the divergence distribution, storms accentuate the left tail, which has been associated with the presence of rain (O'Neill *et al.*, 2017). Moreover, the two pdfs in each panel indicate that, except in summer, the negative tail is higher when wind crosses a front from warm to cold ($\gamma < 0$) than from cold to warm ($\gamma > 0$). This means that the DMM mechanism plays a non-negligible role when a storm, characterised by strong values of convergence, crosses a SST front from warm to cold. The ratio $r_{NN}(\delta)$, especially in April and October, shows that, even accounting for the overall larger number of fronts crossed

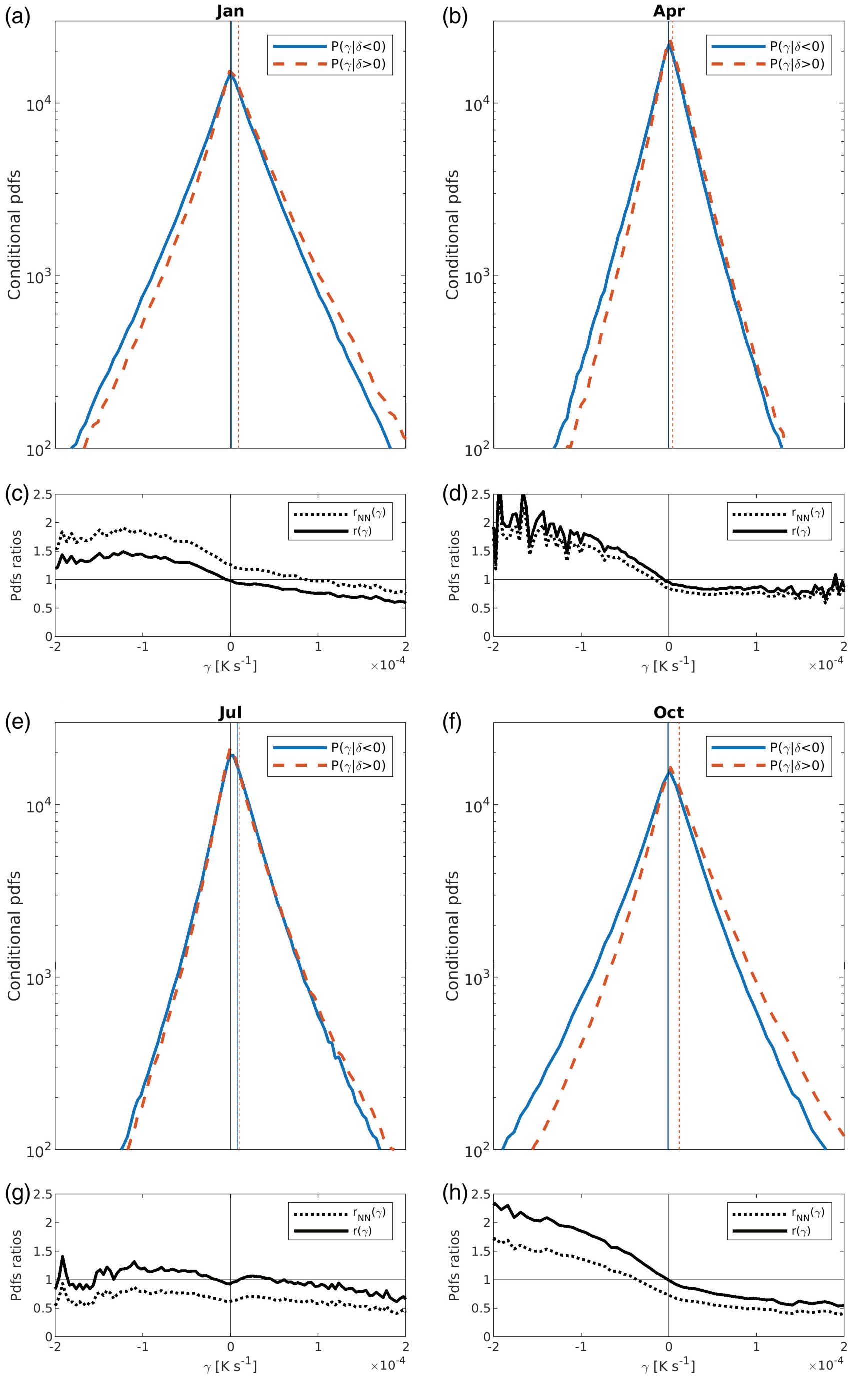

FIGURE 6 Probability density function of downwind SST gradients, conditioned on wind convergence (solid line) and wind divergence (dashed line), for the months of (a) January, (b) April, (e) July and (f) October. Vertical thin lines indicate the mean values (solid for $P(\gamma|\delta < 0)$ and dashed for $P(\gamma|\delta > 0)$) of the distributions. (c, d, g, h) Corresponding ratios of the pdfs. See the text for more details [Colour figure can be viewed at wileyonlinelibrary.com]

from cold to warm usually encountered by winds in the Mediterranean (as shown in Figure 3e, where the area with $\gamma > 0$ is larger than the area with $\gamma < 0$, resulting in $r_{\mathrm{NN}}(\delta) < r(\delta)$, as in Figure 7h), strong convergence is more likely associated with fronts crossed from warm to cold. In summary, we can conclude that, despite the presence of atmospheric frontal systems that certainly influence surface winds masking the wind–SST correlation, strong convergence is particularly sensitive to the underlying SST structure and preferentially occurs when the flow is from warm to cold.

4 | THE ROLE OF THE ATMOSPHERIC SYNOPTIC PATTERNS

When the DMM is effectively in action, SST and wind speed should also be positively correlated. The explanation why this correlation has not been found here is linked to the synoptic-scale atmospheric dynamics. These determine a condition where a weak correlated signal is embedded in a larger background stochastic noise, which is a typical features of many geophysical fluids, as discussed,

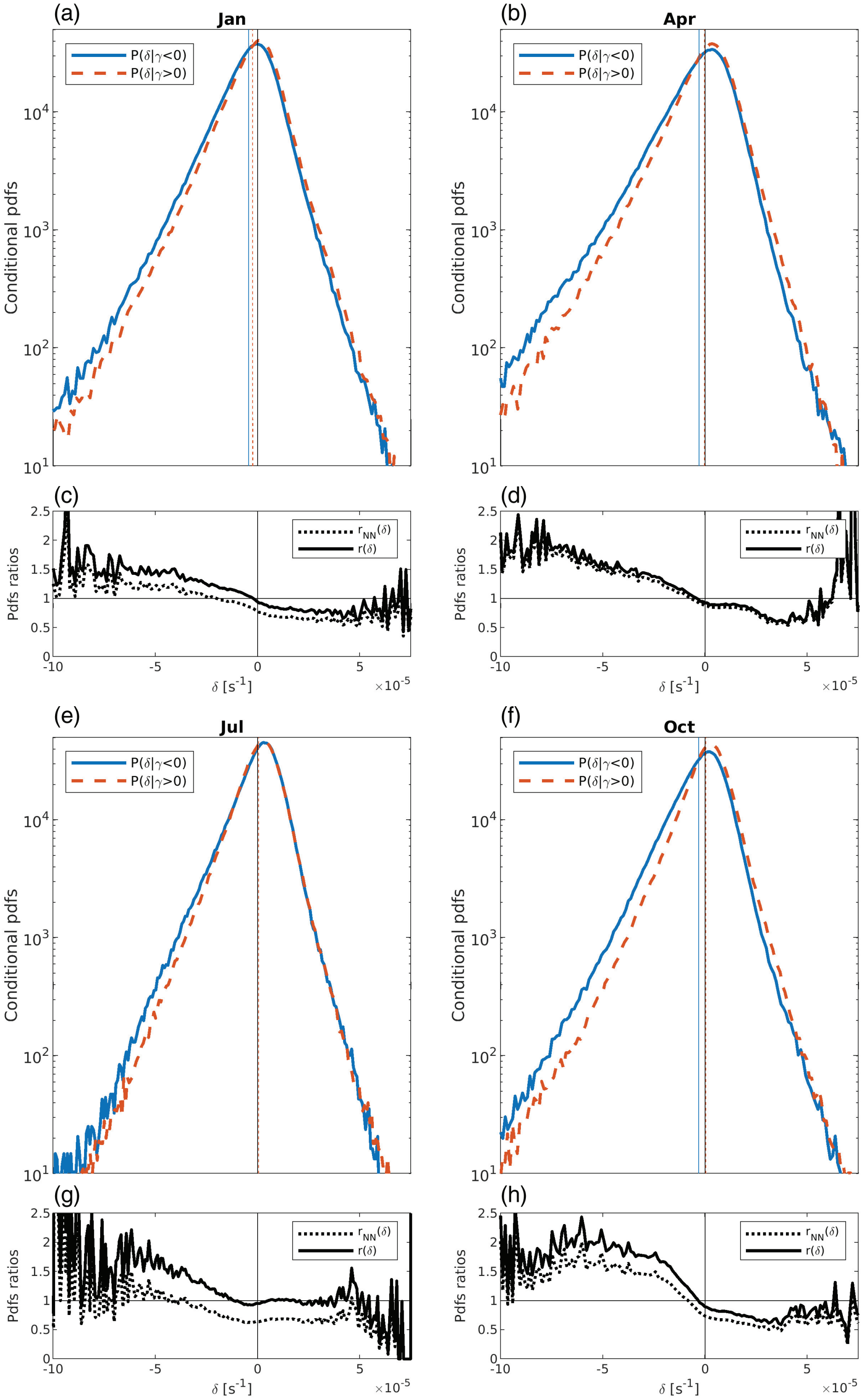

FIGURE 7 As Figure 6, but for probability density function of surface wind divergence, conditioned on the presence of a front crossed from warm to cold (solid line in panels a, b, e, f) and from cold to warm (dashed line in panels a, b, e, f) [Colour figure can be viewed at wileyonlinelibrary.com]

for example, by Plougonven *et al.* (2018). To pursue this concept further, a simple model is here introduced. Consider a non-dimensional temperature anomaly profile $T(x)$ that depends on a single spatial coordinate x. Let $u(x)$ be a non-dimensional wind velocity profile so that

$$u(x) = T(x) + \zeta(x), \tag{7}$$

with $\zeta(x)$ being a random noise correlated in space which mimics the synoptic-scale atmospheric dynamics. Considering the large variations in wind field associated with pressure systems and the large-scale spatial correlation of the wind field, we assume that the noise term is much larger than the temperature term $\mathcal{O}(\zeta) \gg \mathcal{O}(T)$, and that the spatial partial derivatives of the two terms are very

Quarterly Journal of the Royal Meteorological Society RMetS

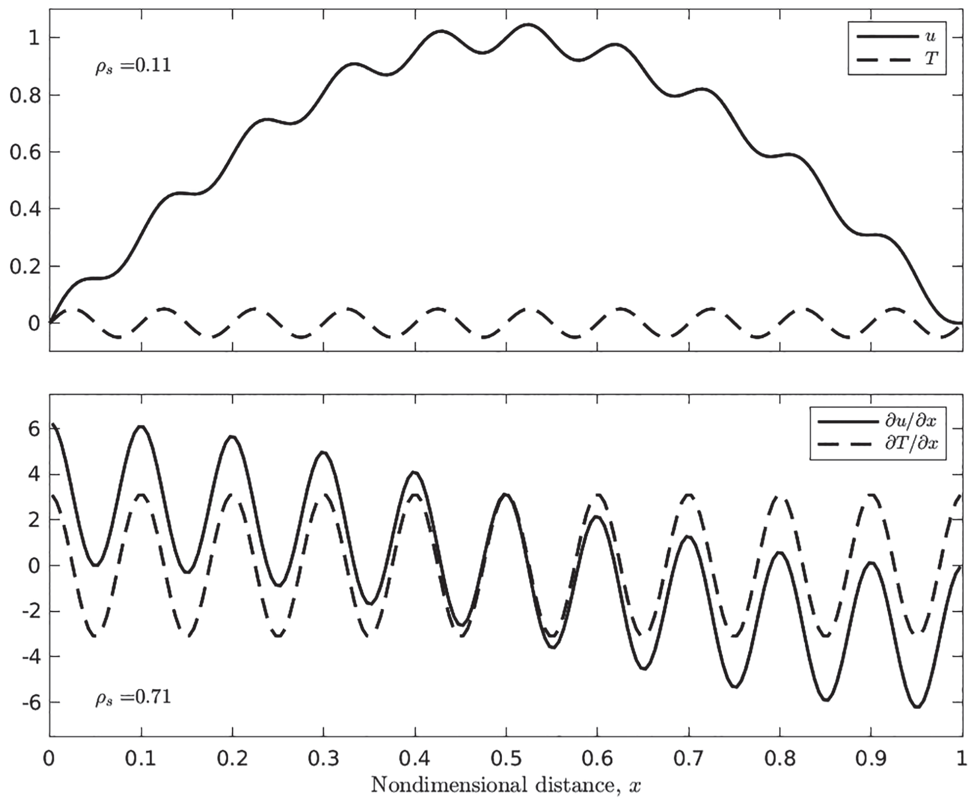

FIGURE 8 The non-dimensional temperature anomaly $T(x)$ is represented as a fast oscillation in space, compared to the large-scale noise $\zeta(x)$. The sum of the two gives the non dimensional wind u(x)=T(x)+ζ(x). The spatial correlation coefficients between the fields represented are shown in each panel. The functions used in the figure are $T = 0.05\sin(20\pi x)$ and $\zeta = \sin(\pi x)$.

different, that is, $\partial_x\zeta(x) \ll \partial_x T(x)$, indicating that the autocorrelation length of the noise is much larger than that of temperature. When calculating the correlation coefficients between u and T, it is then clear that the presence of ζ masks the direct proportionality between the two variables, as $u(x) \simeq \zeta(x)$. Instead, if the spatial derivatives are considered, because of the assumptions above, the noise term drops out, $\partial_x u \simeq \partial_x T$, and the correlation is positive.

In such a simple model, the perfect correlation $u(x) = T(x)$ would be the result of an extremely efficient DMM mechanism, so that SST anomalies completely control surface wind anomalies. Figure 8 depicts a simple situation in which a field composed by the sum of a large-scale signal and a small-scale one is not correlated with the latter, but their spatial derivatives are so.

5 | DISCUSSION AND CONCLUSIONS

Results shown above indicate that over daily time-scales, atmospheric convergence is more likely to occur when wind crosses a SST front from warm to cold. In particular, the use of daily data enabled us to discover, to our knowledge for the first time, that the effect of SST gradients on the surface winds is present and detectable not only under benign weather conditions (weak wind divergences), but also when wind convergence is particularly strong (typically, during intense storms associated with atmospheric frontal dynamics). In fact, in autumn, strong values of convergence are twice as likely to be found over fronts crossed from warm to cold. The relevant process for this link is the mixing of fast-moving air above the marine boundary layer with surface air which is favoured by higher SST which decreases the boundary-layer stability.

The results presented here are in line with a previous numerical work which found that in a midlatitude set-up the DMM mechanism was responsible for the control of the surface winds by the SST structures over $\mathcal{O}(1)$ hr time-scales and $\mathcal{O}(1–100)$ km spatial scales (Meroni *et al.*, 2018). In that work, the fine grid used for the simulations allowed a comparison of the correlation across scales: it was found that the DMM mechanism becomes more efficient for smaller-scale SST structures, down to the km scale. Thus, it is expected that the DMM is even more important in determining the atmospheric response than is found in this work, where the spatial resolution is of the order of a few tens of km.

It should be noted that in this work wind speed is an estimate obtained by scatterometer data, which actually measure the wind stress. Oceanic currents are not considered when converting wind stress into wind speed, resulting in possible inaccuracies (Renault *et al.*, 2019). Moreover, the retrieval algorithm assumes a neutral stability profile in the boundary layer. The obtained equivalent neutral wind has been shown to overestimate (underestimate) the actual near-surface wind in the case of an unstable (stable) boundary layer (O'Neill *et al.*, 2012). On a warm (cold) ocean, the equivalent neutral wind will thus be larger (smaller) than the actual wind. For this reason, the negative correlation found between SST and wind might actually be underestimated. Our results also indicate that there is a preference for convergence (divergence) over fronts crossed from warm to cold (from cold to warm). In this case, the use of the equivalent neutral wind might overestimate the magnitude of both divergence and convergence, and thus resulting in larger correlations with the SST gradients. However, this simply amplifies a signal which is present (O'Neill *et al.*, 2012) without invalidating the main results of this work, i.e. the preferential occurrence of wind convergence over fronts crossed from warm to cold.

Surface wind convergence is typically associated with uprising motion and divergence aloft, favouring cloud formation. If the atmospheric conditions are favourable (i.e., the air column is moist and not too stable), convergence lines can produce precipitation. While it is known that small-scale SST structures do not impact the total amount of precipitation (Millán *et al.*, 1995; Pastor *et al.*, 2001; Lebeaupin *et al.*, 2006; Cassola *et al.*, 2016), our results suggest that, under the appropriate atmospheric stability conditions (yet to be properly studied and determined), they can affect the localisation of precipitation by enhancing the probability of the development of a surface convergence line. While in the open ocean the forecast of the exact location of a heavy precipitation event is generally not particularly relevant for civil protection applications, the correct forecast of convergence lines over the sea and of precipitation can be very important in the presence of islands and in basins with large urbanisation in coastal areas, such as in the Mediterranean region. Even if in coastal regions land–sea contrasts and topographic effects also play a role, our results indicate that the correct representation of small-scale SST structures and of the related air–sea interactions are important aspects in determining the localisation of convergence lines.

To deepen our understanding of the connections between SST fronts and precipitation more analyses are needed. In particular, the long time series provided by atmospheric and oceanic reanalysis datasets could be helpful for this task. By having access to the three-dimensional fields, the role of atmospheric stability could be studied, as well as the depth of the atmospheric boundary layer that reacts to the SST front. In parallel, since results would be dependent on the specific parametrization of air–sea fluxes used in the models, the collection of high-resolution simultaneous retrieval of upper ocean and atmospheric properties would be highly desirable to identify the relevant processes in the air–sea interactions.

ACKNOWLEDGEMENTS

This work is an outcome of Project MIUR – Dipartimenti di Eccellenza 2018–2022. ANM was partially supported by the DARFLIS project of Fondazione Cariplo and by the TWIGA project, which has received funding from the European Union's Horizon 2020 Research and Innovation Programme under grant agreement No.776691. The SSTs used in this work have been obtained from the NOAA daily Optimum Interpolation Sea Surface Temperature dataset (OISST; https://www.ncdc.noaa.gov/oisst; accessed 13 January 2020). The 10 m wind data have been obtained from the Cross-Calibrated Multi-Platform wind vector analysis (CCMPv2.0), available at https://www.remss.com/measurements/ccmp (accessed 13 January 2020).

CONFLICT OF INTEREST

The authors declare no conflict of interest.

ORCID

Agostino N. Meroni https://orcid.org/0000-0001-5504-632X

REFERENCES

Atlas, R., Hoffman, R.N., Ardizzone, J., Leidner, S.M., Jusem, J.C., Smith, D.K. and Gombos, D. (2011) A cross-calibrated, multiplatform ocean surface wind velocity product for meteorological and oceanographic applications. *Bulletin of the American Meteorological Society*, 92, 157–174.

Banzon, V., Smith, T.M., Chin, T.M., Liu, C. and Hankins, W. (2016) A long-term record of blended satellite and *in situ* sea-surface temperature for climate monitoring, modeling and environmental studies. *Earth System Science Data*, 8, 165–176.

Bourras, D., Reverdin, G., Giordani, H. and Caniaux, G. (2004) Response of the atmospheric boundary layer to a mesoscale oceanic eddy in the northeast Atlantic. *Journal of Geophysical Research; Atmospheres*, 109(D18). https://doi.org/10.1029/2004JD004799

Bretherton, C.S., Widmann, M., Dymnikov, V.P., Wallace, J.M. and Bladé, I. (1999) The effective number of spatial degrees of freedom of a time-varying field. *Journal of Climate*, 12, 1990–2009.

Bryan, F.O., Tomas, R., Dennis, J.M., Chelton, D.B., Loeb, N.G. and McClean, J.L. (2010) Frontal scale air–sea interaction in high-resolution coupled climate models. *Journal of Climate*, 23, 6277–6291.

Businger, J.A. and Shaw, W.J. (1984) The response of the marine boundary layer to mesoscale variations in sea-surface temperature. *Dynamics of Atmospheres and Oceans*, 8, 267–281.

Byrne, D., Papritz, L., Frenger, I., Münnich, M. and Gruber, N. (2015) Atmospheric response to mesoscale sea surface temperature anomalies: assessment of mechanisms and coupling strength in a high-resolution coupled model over the South Atlantic. *Journal of the Atmospheric Sciences*, 72, 1872–1890.

Cassola, F., Ferrari, F., Mazzino, A. and Miglietta, M.M. (2016) The role of the sea in the flash floods events over Liguria (northwestern Italy). *Geophysical Research Letters*, 43, 3534–3542. https://doi.org/10.1002/2016GL068265

Chelton, D.B. and Xie, S.P. (2010) Coupled ocean-atmosphere interaction at oceanic mesoscales. *Oceanography*, 23(4), 52–69.

Chelton, D.B., Esbensen, S.K., Schlax, M.G., Thum, N., Freilich, M.H., Wentz, F.J., Gentemann, C.L., McPhaden, M.J. and Schopf, P.S. (2001) Observations of coupling between surface wind stress and sea surface temperature in the eastern tropical Pacific. *Journal of Climate*, 14, 1479–1498.

D'Ortenzio, F., Iudicone, D., de Boyer Montegut, C., Testor, P., Antoine, D., Marullo, S., Santoleri, R. and Madec, G. (2005) Seasonal variability of the mixed layer depth in the Mediterranean Sea as derived from *in situ* profiles. *Geophysical Research Letters*, 32.

De Szoeke, S.P. and Bretherton, C.S. (2004) Quasi-Lagrangian large eddy simulations of cross-equatorial flow in the East Pacific atmospheric boundary layer. *Journal of the Atmospheric Sciences*, 61(15), 1837–1858.

Desbiolles, F., Blamey, R., Illig, S., James, R., Barimalala, R., Renault, L. and Reason, C. (2018) Upscaling impact of wind/sea surface temperature mesoscale interactions on southern Africa austral summer climate. *International Journal of Climatology*, 38, 4651–4660.

Foussard, A., Lapeyre, G. and Plougonven, R. (2019) Response of surface wind divergence to mesoscale SST anomalies under different wind conditions. *Journal of the Atmospheric Sciences*, 76, 2065–2082.

Frenger, I., Gruber, N., Knutti, R. and Münnich, M. (2013) Imprint of Southern Ocean eddies on winds, clouds and rainfall. *Nature Geoscience*, 6, 608–612.

Gaube, P., Chickadel, C.C., Branch, R. and Jessup, A. (2019) Satellite observations of SST-induced wind speed perturbation at the oceanic submesoscale. *Geophysical Research Letters*, 46, 2690–2695.

Hashizume, H., Xie, S.P., Liu, W.T. and Takeuchi, K. (2001) Local and remote atmospheric response to tropical instability waves: a global view from space. *Journal of Geophysical Research*, 106, 10173–10185.

Hayes, S.P., McPhaden, M.J. and Wallace, J.M. (1989) The influence of sea surface temperature on surface wind in the eastern equatorial Pacific. *Journal of Climate*, 2, 1500–1506.

Hoffman, R.N., Henderson, J.M., Atlas, R. and Ardizzone, J.V. (2003) A two-dimensional variational analysis method for NSCAT ambiguity removal: methodology, sensitivity, and tuning. *Journal of Atmospheric and Oceanic Technology*, 20, 585–605.

Iizuka, S. and Nakamura, H. (2019) Sensitivity of midlatitude heavy precipitation to SST: a case study in the sea of Japan area on 9 August 2013. *Journal of Geophysical Research: Atmospheres*, 124, 4365–4381. https://doi.org/10.1029/2018JD029503

Katsafados, P., Mavromatidis, E., Papadopoulos, A. and Pytharoulis, I. (2011) Numerical simulation of a deep Mediterranean storm and its sensitivity on sea surface temperature. *Natural Hazards and Earth System Sciences*, 11, 1233–1246.

Kilpatrick, T., Schneider, N. and Qiu, B. (2014) Boundary-layer convergence induced by strong winds across a midlatitude SST front. *Journal of Climate*, 27, 1698–1718.

Lebeaupin, C., Ducrocq, V. and Giordani, H. (2006). *Journal of Geophysical Research*, 111(D12). https://doi.org/10.1029/2005JD006541

Li, Y. and Carbone, R.E. (2012) Excitation of rainfall over the tropical western Pacific. *Journal of the Atmospheric Sciences*, 69, 2983–2994.

Lindzen, R.S. and Nigam, R.S. (1987) On the role of the sea surface temperature gradients in forcing low-level winds and convergence in the tropics. *Journal of the Atmospheric Sciences*, 44, 2418–2436.

Liu, W.T., Xie, X., Polito, P.S., Xie, S.P. and Hashizume, H. (2000) Atmospheric manifestation of tropical instability wave observed by QuikSCAT and tropical rain measuring mission. *Geophysical Research Letters*, 27, 2545–2548.

Ma, J., Xu, H., Dong, C., Lin, P. and Liu, Y. (2015) Atmospheric responses to oceanic eddies in the Kuroshio Extension region. *Journal of Geophysical Research: Atmospheres*, 120, 6313–6330.

Meroni, A.N., Parodi, A. and Pasquero, C. (2018) Role of SST patterns on surface wind modulation of a heavy midlatitude precipitation event. *Journal of Geophysical Research: Atmospheres*, 123, 9081–9096.

Messager, C., Speich, S. and Key, E. (2012) Marine atmospheric boundary layer over some Southern Ocean fronts during the IPY BGH 2008 cruise. *Ocean Science*, 8, 1001–1023.

Messager, C. and Swart, S. (2016) Significant atmospheric boundary layer change observed above an Agulhas current warm cored eddy. *Advances in Meteorology*, 2016. https://doi.org/10.1155/2016/3659657

Millán, M.M., Estrela, J. and Caselles, V. (1995) Torrential precipitations on the Spanish east coast: the role of the Mediterranean sea-surface temperature. *Atmospheric Research*, 36, 1–16.

Minobe, S., Kuwano-Yoshida, A., Komori, N., Xie, S.-P. and Small, R.J. (2008) Influence of the Gulf Stream on the troposphere. *Nature*, 452, 206–209.

Minobe, S., Miyashita, M., Kuwano-Yoshida, A., Tokinaga, H. and Xie, S.-P. (2010) Atmospheric response to the Gulf Stream: seasonal variations. *Journal of Climate*, 23, 3699–3719.

O'Neill, L.W., Chelton, D.B. and Esbensen, S.K. (2012) Covariability of surface wind and stress responses to sea surface temperature fronts. *Journal of Climate*, 25, 5916–5942.

O'Neill, L.W., Chelton, D.B., Esbensen, S.K. and Wentz, F.J. (2005) High-resolution satellite measurements of the atmospheric boundary-layer response to SST variations along the Agulhas return current. *Journal of Climate*, 18, 2706–2723.

O'Neill, L.W., Haack, T., Chelton, D.B. and Skyllingstad, E. (2017) The Gulf Stream convergence zone in the time-mean winds. *Journal of the Atmospheric Sciences*, 74, 2383–2412.

Park, K.A., Cornillon, P. and Codiga, D.L. (2006) Modification of surface winds near ocean fronts: effects of Gulf Stream rings on scatterometer (QuickSCAT, NSCAT) wind observations. *Journal of Geophysical Research: Oceans*, 111(C3). https://doi.org/10.1029/2005JC003016

Pastor, F., Estrela, M.J., narrocha, D.P. and Millán, M.M. (2001) Torrential rains on the Spanish Mediterranean coast: modeling the effects of the sea surface temperature. *Journal of Applied Meteorology*, 40, 1180–1195.

Plougonven, R., Foussard, A. and Lapeyre, G. (2018) Comments on "The Gulf Stream convergence zone in the time-mean winds". *Journal of the Atmospheric Sciences*, 75, 2139–2149.

Press, W.H., Teukolsky, S.A., Vetterling, W.T. and Flannery, B.P. (1992) *Numerical Recipes in C* (2nd ed.) Cambridge University Press, Cambridge, UK.

Rainaud, R., Lebeaupin Brossier, C., Ducrocq, V. and Giordani, H. (2017) High-resolution air–sea coupling impact on two heavy precipitation events in the Western Mediterranean. *Quarterly Journal of the Royal Meteorological Society*, 143, 2448–2462.

Renault, L., Masson, S., Oerder, V., Jullien, S. and Colas, F. (2019) Disentangling the mesoscale ocean–atmosphere interactions. *Journal of Geophysical Research: Oceans*, 124(3), 2164–2178. https://doi.org/10.1029/2018JC014628

Renault, L., McWilliams, J.C. and Gula, J. (2018) Dampening of submesoscale currents by air–sea stress coupling in the Californian upwelling system. *Scientific Reports*, 8(13388). https://doi.org/10.1038/s41598-018-31602-3

Ricchi, A., Miglietta, M.M., Falco, P.P., Benetazzo, A., Bonaldo, D., Bergamasco, A., Sclavo, M. and Carniel, S. (2016) On the use of a coupled ocean–atmosphere–wave model during an extreme cold air outbreak over the Adriatic Sea. *Atmospheric Research*, 172–173, 48–65. https://doi.org/10.1016/j.atmosres.2015.12.023

Roberts, M.J., Hewitt, H.T., Hyder, P., Ferreira, D., Josey, S.A., Mizielinski, M. and et al. (2016) Impact of ocean resolution on coupled air–sea fluxes and large-scale climate. *Geophysical Research Letters*, 43, 10430–10438. https://doi.org/10.1002/2016GL070559

Rouault, M., Verley, P. and Backeberg, B. (2016) Wind changes above warm Agulhas current eddies. *Ocean Science*, 12, 495–506.

Scott, J.P., Wentz, F.J., Hoffman, R.N. and Atlas, R. (2016). Improvements and advances to the cross-calibrated multi-platform (CCMP) ocean vector wind analysis (V2.0 release). presented at the: AGU Ocean Sciences Meeting, 21–26 February 2016, New Orleans, LA.

Seo, H. (2017) Distinct influence of air–sea interactions mediated by mesoscale sea surface temperature and surface current in the Arabian Sea. *Journal of Climate*, 30, 8061–8080.

Skyllingstad, E.D., Vickers, D. and Mahrt, L. (2007) Effects of mesoscale sea-surface temperature fronts on the marine atmospheric boundary layer. *Boundary-Layer Meteorology*, 123, 219–237.

Small, R.J., deSzoeke, S.P., Xie, S.P., O'Neilland, H., Seo, L., Song, Q., Cornillon, P., Spall, M. and Minobe, S. (2008) Air–sea interaction over ocean fronts and eddies. *Dynamics of Atmospheres and Oceans*, 45, 274–319. https://doi.org/10.1016/j.dynatmoce.2008.01.001

Song, Q., Cornillon, P. and Hara, T. (2006) Surface wind response to oceanic fronts. *Journal of Geophysical Research: Oceans*, 111(C12). https://doi.org/10.1029/2006JC003680

Spall, M.A. (2007) Midlatitude wind stress-sea surface temperature coupling in the vicinity of oceanic fronts. *Journal of Climate*, 20, 3785–3801.

Sun, S., Fang, Y., Liu, B. and Tana, C. (2016) Coupling between SST and wind speed over mesoscale eddies in the South China Sea. *Ocean Dynamics*, 66, 1467–1474.

Wallace, J.M., Mitchell, T.P. and Deser, C. (1989) The influence of sea surface temperature on surface wind in the eastern equatorial Pacific: seasonal and interannual variability. *Journal of Climate*, 2, 1492–1499.

Wang, Y. and Castelao, R.M. (2016) Variability in the coupling between sea surface temperature and wind stress in the global coastal ocean. *Continental Shelf Research*, 125, 88–96.

Wenegrat, J.O. and Arthur, R.S. (2018) Response of the atmospheric boundary layer to submesoscale sea surface temperature fronts. *Geophysical Research Letters*, 45, 13505–13512.

Wentz, F.J., Scott, J., Hoffman, R., Leidner, M., Atlas, R. and Ardizzone, J. (2015) *Remote Sensing Systems Cross-Calibrated Multi-Platform (CCMP) 6-hourly Ocean Wind Vector Wind Analysis Product on 0.25 deg grid, version 2.0*. Remote Sensing Systems, Santa Rosa, CA. http://www.remss.com/measurements/ccmp/; accessed 13 January 2020.

Xie, S.P. (2004) Satellite observations of cool ocean–atmosphere interaction. *Bulletin of the American Meteorological Society*, 85, 195–208.

Xie, S.P., Ishiwatari, M., Hashizume, H. and Takeuchi, K. (1998) Coupled ocean–atmospheric waves on the equatorial front. *Geophysical Research Letters*, 25, 3863–3866.

Zecchetto, S. and Cappa, C. (2001) The spatial structure of the Mediterranean Sea winds revealed by ERS-1 scatterometer. *International Journal of Remote Sensing*, 22, 45–70.

How to cite this article: Meroni AN, Giurato M, Ragone F, Pasquero C. Observational evidence of the preferential occurrence of wind convergence over sea surface temperature fronts in the Mediterranean. *Q J R Meteorol Soc*. 2020;146:1443–1458. https://doi.org/10.1002/qj.3745

APPENDIX: STATISTICAL DEFINITIONS AND METHODS

Given two generic fields $a(\varphi, \theta)$ and $b(\varphi, \theta)$ defined on a regular grid in spherical coordinates, their instantaneous spatial correlation coefficient is

$$\rho_s[a,b] = \frac{1}{\sigma_a \sigma_b |\Omega|} \iint_\Omega R^2 \cos\theta \left[a(\varphi,\theta) - \overline{a}\right] \times \left[b(\varphi,\theta) - \overline{b}\right] \mathrm{d}\varphi \, \mathrm{d}\theta, \tag{A1}$$

where

$$\overline{a} = \frac{1}{|\Omega|} \iint_\Omega R^2 \cos\theta \; a(\varphi,\theta) \; \mathrm{d}\varphi \, \mathrm{d}\theta \tag{A2}$$

is the spatial mean of the field $a(\varphi, \theta)$ and

$$\sigma_a^2 = \frac{1}{|\Omega|} \iint_\Omega R^2 \cos\theta \; \left[a(\varphi,\theta) - \overline{a}\right]^2 \mathrm{d}\varphi \, \mathrm{d}\theta \tag{A3}$$

its spatial variance over the region Ω, with

$$|\Omega| = \iint_\Omega R^2 \cos\theta \; \mathrm{d}\varphi \, \mathrm{d}\theta \tag{A4}$$

its area.

Pointwise, the temporal correlation coefficients between two time-dependent quantities $a(t)$ and $b(t)$ is

$$\rho_t[a,b] = \frac{1}{\sigma_a^* \sigma_b^* |\omega|} \int_\omega \left[a(t) - \overline{a}^*\right] \left[b(t) - \overline{b}^*\right] \mathrm{d}t, \quad \text{(A5)}$$

where

$$\overline{a}^* = \frac{1}{|\omega|} \int_\omega a(t)\, \mathrm{d}t \quad \text{(A6)}$$

is the temporal mean of the variable $a(t)$ and

$$\sigma_a^{*2} = \frac{1}{|\omega|} \int_\omega \left[a(t) - \overline{a}^*\right]^2 \mathrm{d}t \quad \text{(A7)}$$

its temporal variance over the time interval ω, with duration

$$|\omega| = \int_\omega \mathrm{d}t. \quad \text{(A8)}$$

To assess the significance of the correlation coefficients, the 95% confidence interval of the null hypothesis of zero correlation is calculated using the effective number of degrees of freedom, following Press *et al.* (1992) and Bretherton *et al.* (1999). In the first place, for the spatial correlation coefficients, the autocorrelation lengths of both the downwind SST gradient and the surface wind divergence are calculated. In particular, for a field $q(\varphi, \theta)$, the bidimensional autocorrelation function is

$$\mathcal{A}_q(\xi, \eta) = \frac{1}{\sigma_q^2 |\Omega|} \iint_\Omega R^2 \cos\theta \left[q(\varphi, \theta) - \overline{q}\right] \times \left[q\left(\varphi + \frac{\xi}{R\cos\theta}, \theta + \frac{\eta}{R}\right) - \overline{q}\right] \mathrm{d}\varphi\, \mathrm{d}\theta, \quad \text{(A9)}$$

where $\{\xi, \eta\}$ is a set of local Cartesian coordinates. The isotropic autocorrelation function $A_q(r)$ is found in a set of local polar coordinates $\{r, \delta\}$, with r being the radial distance from the origin and δ being the counterclockwise angle from the positive ξ axis, by averaging over full circles, namely

$$A_q(r) = \frac{1}{2\pi} \int_0^{2\pi} \mathcal{A}_q(r\cos\delta, r\sin\delta)\, \mathrm{d}\delta. \quad \text{(A10)}$$

Once $A_q(r)$ is known, the autocorrelation length λ_q is the distance at which

$$A_q(\lambda_q) = \mathrm{e}^{-1}. \quad \text{(A11)}$$

The autocorrelation lengths are calculated for both variables and the smallest between the two, denoted by λ, is saved. This is done for the entire duration of the dataset and it is found that the autocorrelation length of the downwind SST gradient is systematically smaller than that of the surface wind divergence. The temporal mean of λ, denoted by $\overline{\lambda}^*$, is found to be $\overline{\lambda}^* = 84$ km and it is used to calculate the number of effective degrees of freedom following Bretherton *et al.* (1999) as

$$N_s = \frac{|\Omega|}{\overline{\lambda}^{*2}} = 224, \quad \text{(A12)}$$

with the area of the basin of interest $|\Omega| = 1{,}567{,}442$ km^2. The standard deviation of the null hypothesis is then $\sigma_0 = 1/\sqrt{N_s} = 6.7 \times 10^{-2}$ (Press *et al.*, 1992). In order to evaluate the 95% confidence level of the mean value of the correlation coefficient, its standard error has to be estimated. Considering that the temporal autocorrelation length in our dataset is 2 days (see below), the number of independent repetitions in a representative month of 30 days over 25 years is $N_t = 375$. Thus, the 95% confidence interval on the mean correlation coefficient is estimated to be $1.96\sigma_0/\sqrt{N_t} = 6.7 \times 10^{-3}$.

For the spatial correlation between wind speed and SST, the width of the 95% confidence interval is 3×10^{-2}, based on the number of effective degrees of freedom $N_s = 11$, derived using the autocorrelation length of the SST equal to 371 km and $N_t = 375$, since the relevant temporal autocorrelation length is also 2 days here.

For the spatial correlation between SST Laplacian and wind divergence, the 95% confidence level is found as $1.96/\sqrt{N_s N_t} = 5.9 \times 10^{-3}$, where $N_s = 440$ is here calculated with an autocorrelation length of 60 km, characteristic of the SST Laplacian field, and $N_t = 250$, calculated considering a representative month of 30 days over 25 years of data, with a temporal autocorrelation length of 3 days.

For the calculation of the confidence interval of the temporal correlation coefficients, a similar procedure is followed. Taking the entire duration of the dataset, the temporal autocorrelation function is calculated pointwise for each variable. In particular, the Wiener–Khinchin theorem, which affirms that the autocorrelation function and the power spectral density are a Fourier transform pair, is exploited (Press *et al.*, 1992). The temporal autocorrelation length is then calculated pointwise and averaged in space both for $\nabla \cdot \mathbf{u}$ and $\mathbf{u} \cdot \nabla$SST. In this case the smallest value is for $\mathbf{u} \cdot \nabla$SST, and denoted by $\overline{\lambda} = 2$ days. The number of effective degrees of freedom for a certain interval of the dataset with duration ω is

$$N_t = \frac{\omega}{\overline{\lambda}} = 1138, \quad \text{(A13)}$$

considering the autumn season for 25 years ($\omega = 2275$ days). The standard deviation of the null hypothesis is found as $\sigma_0^* = 1/\sqrt{N_t} = 3 \times 10^{-2}$, which, since the significance of each correlation coefficient is evaluated, leads to a 95% confidence interval equal to $1.96\sigma_0^* = 5.8 \times 10^{-2}$. This is the value used to assess the significance of the results shown in Figure 5a,b.

A different confidence interval level is associated with the temporal correlation between SST Laplacian and wind divergence, Figure 5c, because the temporal autocorrelation length of interest is of 3 days (typical of the surface divergence field), which leads to a number of effective degrees of freedom $N_\mathrm{t} = 1138$ and a confidence interval of 5.8×10^{-2}.